

A multi-dimensional Vlasov-Fokker-Planck code for arbitrarily anisotropic high-energy-density plasmas

M. Tzoufras, A. Tableman, F. S. Tsung, W. B. Mori, and A. R. Bell

Citation: [Physics of Plasmas](#) **20**, 056303 (2013); doi: 10.1063/1.4801750

View online: <https://doi.org/10.1063/1.4801750>

View Table of Contents: <http://aip.scitation.org/toc/php/20/5>

Published by the [American Institute of Physics](#)

Articles you may be interested in

[Electron holes in phase space: What they are and why they matter](#)

[Physics of Plasmas](#) **24**, 055601 (2017); 10.1063/1.4976854

[Simulation of self-generated magnetic fields in an inertial fusion hohlraum environment](#)

[Physics of Plasmas](#) **24**, 052703 (2017); 10.1063/1.4983140

[A comparison of non-local electron transport models for laser-plasmas relevant to inertial confinement fusion](#)

[Physics of Plasmas](#) **24**, 082706 (2017); 10.1063/1.4986095

[Interaction of a highly radiative shock with a solid obstacle](#)

[Physics of Plasmas](#) **24**, 082707 (2017); 10.1063/1.4996010

[Particle-in-cell simulations of an RF emission mechanism associated with hypervelocity impact plasmas](#)

[Physics of Plasmas](#) **24**, 053102 (2017); 10.1063/1.4980833

[Resonance between heat-carrying electrons and Langmuir waves in inertial confinement fusion plasmas](#)

[Physics of Plasmas](#) **23**, 012707 (2016); 10.1063/1.4939603

**PHYSICS
TODAY**

**COMPLETELY
REDESIGNED!**

Physics Today Buyer's Guide
Search with a purpose.

A multi-dimensional Vlasov-Fokker-Planck code for arbitrarily anisotropic high-energy-density plasmas^{a)}

M. Tzoufras,^{1,b)} A. Tableman,¹ F. S. Tsung,¹ W. B. Mori,¹ and A. R. Bell²

¹Department of Physics and Astronomy, University of California, Los Angeles, California 90095, USA

²Clarendon Laboratory, University of Oxford, Parks Road, Oxford OX1 3PU, United Kingdom and Central Laser Facility, STFC Rutherford-Appleton Laboratory, Chilton, Didcot, Oxfordshire OX11 0QX, United Kingdom

(Received 30 November 2012; accepted 5 February 2013; published online 16 April 2013)

To study the kinetic physics of High-Energy-Density Laboratory Plasmas, we have developed the parallel relativistic 2D3P Vlasov-Fokker-Planck code OSHUN. The numerical scheme uses a Cartesian mesh in configuration-space and incorporates a spherical harmonic expansion of the electron distribution function in momentum-space. The expansion is truncated such that the necessary angular resolution of the distribution function is retained for a given problem. Finite collisionality causes rapid decay of the high-order harmonics, thereby providing a natural truncation mechanism for the expansion. The code has both fully explicit and implicit field-solvers and employs a linearized Fokker-Planck collision operator. OSHUN has been benchmarked against well-known problems, in the highly kinetic limit to model collisionless relativistic instabilities, and in the hydrodynamic limit to recover transport coefficients. The performance of the code, its applicability, and its limitations are discussed in the context of simple problems with relevance to inertial fusion energy. © 2013 AIP Publishing LLC. [<http://dx.doi.org/10.1063/1.4801750>]

I. INTRODUCTION

A. Ubiquity of kinetic effects in laser-ablated plasmas

The transport of electrons through ionized matter is a basic science and engineering problem, with applications ranging from fusion plasmas, to astrophysics, to semiconductor technology. In each case, one needs to employ a model that incorporates the essential physics of the background material and the laws that govern its interaction with the flow of electrons. The main challenge in developing an accurate simulation capability is finding a simple enough set of rules that retains the pertinent features of the interaction, because a full description of the microscopic physics of individual electron trajectories for large spatial and temporal scales is not currently feasible even on the world's largest computers. Furthermore, even if such calculations become possible they will not be the most efficient way to study the microphysics for many scenarios.

Laser-ablated plasmas typically involve materials with maximum density in excess of solid, that is, 10^{23} cm^{-3} , ionized by sub- μm , pico-second to nano-second pulses. Laser energy is absorbed in the under-dense corona up to the critical density, $n_c \simeq 9.0663 \times 10^{21} \text{ cm}^{-3} \times (0.351 \mu\text{m}/\lambda_0)^2$, where λ_0 is the laser wavelength, and then conducted deeper in the target by electrons. To a first approximation, the plasma can be described as a fluid and heat conduction can be considered a local diffusion process that obeys Fourier's law, $Q_e = \kappa_{SH} \nabla T_e$, where Q_e is the heat flux and κ_{SH} the effective heat conduction coefficient calculated by Spitzer and Härm for a fully ionized plasma.²⁷ This is a straightforward and

attractive approach, but it assumes that the electron distribution function remains Maxwellian everywhere and that the scale-length of the electron temperature is long compared to the collisional mean free path.

Non-Maxwellian distributions are, however, prevalent in HEDLP. For example, even for moderate intensities, laser absorption due to inverse bremsstrahlung is associated with the Dum^{11,12}-Langdon¹⁹-Matte²³ distributions. For higher intensities, the absorption is dominated by parametric instabilities which produce distributions with high-energy tails. If the intensity increases further more exotic mechanisms can occur, that cause extreme distortions to the electron distribution. Meanwhile, even in a fully Maxwellian plasma, the presence of a steep temperature gradient generates non-Maxwellian features as energetic particles outrun the slower ones. Moreover, these kinetic phenomena do not appear in isolation; the distribution function generated from the absorption of an intense laser pulse determines the characteristics of the electron transport and vice-versa.

B. Vlasov-Fokker-Planck modeling for non-Maxwellian plasmas

1. The Vlasov-Fokker-Planck equation

When the correlations between the fluctuating fields are small, the evolution of a distribution of charged particles $f(\mathbf{r}, \mathbf{p}, t)$ can be described by the Boltzmann equation

$$\frac{\partial f}{\partial t} + \mathbf{v} \cdot \frac{\partial f}{\partial \mathbf{r}} + q \left(\mathbf{E} + \frac{\mathbf{v}}{c} \times \mathbf{B} \right) \cdot \frac{\partial f}{\partial \mathbf{p}} = \left(\frac{\delta f}{\delta t} \right)_c, \quad (1)$$

where \mathbf{E} and \mathbf{B} represent the ensemble-averaged fields and $\left(\frac{\delta f}{\delta t} \right)_c$ the change in the distribution function due to collisions. For a collisionless plasma, one can set $\left(\frac{\delta f}{\delta t} \right)_c = 0$ to

^{a)}Paper YI2 3, Bull. Am. Phys. Soc. 57, 369 (2012).

^{b)}Invited speaker. Electronic mail: mtzoufras@physics.ucla.edu.

obtain the entropy-conserving Vlasov equation. In a plasma with large number of particles in a Debye sphere $N_D = (4/3)n\lambda_D^3 = (4/3)n(k_B T_e / 4\pi n q)^{3/2} \gg 1$, but not so large as to render the plasma collisionless, the cumulative effect of many distant interactions dominates the collision operator which may be written as a conservation equation

$$\left(\frac{\delta f}{\delta t}\right)_{FP} = -\frac{\partial}{\partial \mathbf{v}} \cdot [f \langle \Delta \mathbf{v} \rangle] + \frac{1}{2} \frac{\partial}{\partial \mathbf{v}} \frac{\partial}{\partial \mathbf{v}} : [f \langle \Delta \mathbf{v} \Delta \mathbf{v} \rangle], \quad (2)$$

where $\Delta \mathbf{v}$ is the velocity increment per unit time. This is the Fokker-Planck collision operator. A compact expression for this collision operator that is amenable to numerical solution was derived by Rosenbluth *et al.*²⁶ under the assumption that changes in velocity are due to binary Coulomb interactions. Substitution of the Fokker-Planck equation into Boltzmann's equation yields the Vlasov-Fokker-Planck equation

$$\frac{\partial f}{\partial t} + \mathbf{v} \cdot \frac{\partial f}{\partial \mathbf{r}} + q \left(\mathbf{E} + \frac{\mathbf{v}}{c} \times \mathbf{B} \right) \cdot \frac{\partial f}{\partial \mathbf{p}} = \left(\frac{\delta f}{\delta t}\right)_{FP}. \quad (3)$$

This equation encompasses much of the kinetic physics of interest to HEDLP, because it describes the evolution of an arbitrary distribution function in the presence of both electromagnetic fields and small-angle binary collisions.

2. Exploitation of spherical geometry from VFP codes

Vlasov-Fokker-Planck codes solve Eq. (3) to simulate the evolution of the electron distribution function, which is a four- to six-dimensional quantity for a one- to three-dimensional configuration-space, respectively. VFP simulations, therefore, demand large amounts of computer memory which, in practice, limits the number of time-steps that can be taken. To get around this, some property of the system is usually exploited, either to shrink the volume of the required information or to solve a reduced set of equations and take large time-steps (or both).

The “diffusive approximation” relies on angular scattering to maintain near-isotropy in momentum-space, while relaxation to a Maxwellian is not assumed. The distribution function may then be expressed as a sum of the isotropic distribution $f_0(p)$, where $p \equiv |\mathbf{p}|$, and a perturbation $f_1(p)$ multiplied by the direction cosines

$$f(\mathbf{p}) \simeq f_0(p) + \frac{\mathbf{p}}{p} \cdot \mathbf{f}_1(p). \quad (4)$$

Thus, the entire 3D momentum-space can be represented with four 1D arrays, containing f_0 and \mathbf{f}_1 . However, only weakly anisotropic phenomena can be captured by this scheme; any anisotropic physics must occur in time-scales that are much longer than the characteristic time for momentum isotropization due to electron-ion collisions, $\tau_{ei} = \tau_e / Z = \frac{3\sqrt{m_e}(k_B T_e)^{3/2}}{4\sqrt{2}\pi n_e e^4 \ln \Lambda}$. This stringent restriction on the shape of the distribution notwithstanding, diffusive VFP simulations in 1D^{4,8,22,28} and 2D^{15–18,29} have been successful in revealing many features of non-local electron transport.

The expansion to spherical harmonics, of which the diffusive approximation is the first-order truncation, allows for

a complete representation of the electron distribution function

$$f(\mathbf{r}, \mathbf{p}, t) = \sum_{\ell=0}^{\infty} \sum_{m=-\ell}^{\ell} f_{\ell}^m(\mathbf{r}, \mathbf{p}, t) P_{\ell}^{|m|}(\cos \theta) e^{im\phi}, \quad (5)$$

where $f_{\ell}^{-m} = (f_{\ell}^m)^*$, $P_{\ell}^{|m|}(x)$ are the associated Legendre polynomials, and we follow the same conventions as in Tzoufras *et al.*,³² that is $(p_x, p_y, p_z) = (p \cos \theta, p \sin \theta \cos \phi, p \sin \theta \sin \phi)$. This expansion must be terminated for some (ℓ_0, m_0) such that the remainder of the series for $(\ell > \ell_0, \text{ or } m > m_0)$ is negligible.

Small-angle angular scattering yields a rate of decay $\gamma_d \propto \ell(\ell+1)/v^3$ for the amplitudes of the spherical harmonics f_{ℓ}^m . Hence, convergence can be ensured for a given momentum value as long as sufficient harmonics are included. This property offers the key justification for using the expansion (5). The more collisional the plasma, and the lower the momenta of interest, the fewer terms are required. However, the truncated expansion becomes increasingly brittle for large momenta, because for any specific spherical harmonic the decay rate vanishes as v^{-3} . To determine (ℓ_0, m_0) one must first decide what part of the momentum-space is important, and then perform a convergence study in this region. Hence, systems involving energetic particles require a large number of terms in the expansion, even if the bulk of the plasma is accurately described by the diffusive approximation. This will be discussed extensively in Sec. III.

3. Synergies between VFP codes and other kinetic approaches

An accurate method for incorporating non-local electron transport in a hydrodynamic framework is crucial to modeling laser-irradiated plasmas. Yet, after more than three decades of research, a universally accepted model remains elusive. In fluid codes, a flux limiter $f < 1$ is often introduced to prevent the heat flux Q_e due to a sharp temperature gradient from exceeding the “free-streaming heat flux” $Q_f = n_e T_e v_t$, i.e., the flux that would result if all of the electrons were to free stream at their thermal velocity $v_t = \sqrt{k_B T_e / m_e}$. The heat conduction equation may then be written as $Q_e = f \kappa_{SH} \nabla T_e$. This heuristic approach artificially bottles up the hot-electron energy that would otherwise be carried by non-local electrons far from the hot region. Improved models rely on the convolution of the local heat flux with a non-local kernel that may be derived analytically or inferred from VFP simulations.¹³ This convolution approach, formulated by Bell² and first incarnated by Luciani *et al.*,²⁰ can capture features of both the flux inhibition and the preheat associated with hot electrons. However, it is only strictly valid for small temperature variations and for time-independent problems, which excludes virtually all laser-irradiated plasmas. Application of such a non-local transport model must therefore be properly justified, especially because different methods can exhibit markedly different behavior outside the sanctioned regime.

The development of Vlasov-Fokker-Planck codes has largely been driven by the imperative of providing an

accurate description for non-local heat conduction in Inertial Confinement Fusion (ICF) plasmas (see Thomas *et al.*³⁰ and references therein). VFP codes can be used to benchmark the non-local electron transport models, or to replace them altogether, by adding a VFP species to a hydro code. The latter may be an overkill, because it saddles the hydro code with a powerful but computationally intensive kinetic code “merely” to get the heat conduction right. The reverse is more common, fluid ions can be incorporated into a VFP code³ to facilitate kinetic simulations over timescales for which ion motion can play a role.

Another way of incorporating kinetic effects into fluid codes is using the Particle-In-Cell approach. Instead of describing the plasma in terms of ensemble-averaged fields it models a single ensemble of finite-size particles. A modified collision operator exists for the interaction between finite-size particles, such that a Boltzmann equation can be derived following the standard methods for point particles, and thermal fluctuations can also be calculated. Thus, PIC simulations allow instabilities to grow from “noise.” Nevertheless, when the Vlasov-Fokker-Planck Eq. (3) is the appropriate representation of the plasma, VFP codes are an attractive way of solving it, particularly in situations where the noise source is not critical. Whereas VFP and PIC are complementary approaches, coupling the two is also possible. For example, a PIC species of super-hot particles can be added to a background of weakly non-Maxwellian plasma that is described by the VFP equation.

Until recently, the ability to develop and apply VFP codes had been limited due to the lack of computational resources. The advent of parallel computer clusters in the last decade, and especially the last few years, opens the way for dispensing with assumptions on the shape of the distribution function and performing multi-dimensional VFP simulations with highly structured momentum-space.

4. Status of VFP codes

The most common VFP codes are those that employ the spherical harmonic expansion—or the formally equivalent approach of the Cartesian tensor expansion—in momentum-space. For the diffusive approximation, both the formalism and numerical techniques are robust and well-tested and a number of such codes are currently being used to study the modification of electron transport due to non-local effects.^{4,8,15–18,22,28,29}

A more detailed representation of the distribution function requires the KALOS⁵ formalism which describes the effect of advection and electromagnetic fields on each spherical harmonic. The implementation of these equations is considerably more involved than those in the diffusive approximation, even in a fully explicit scheme. A code based on this scheme was described in Tzoufras *et al.*³² and will be further discussed here in the context of HEDLP. The KALOS approach is also being applied to the study of cosmic ray acceleration⁶ and a new multi-dimensional hybrid MHD-VFP code, where the VFP species is used for the cosmic rays, has been recently developed by Reville and Bell.²⁵

In contrast, fully Cartesian codes facilitate use of fast algorithms, but because they do not attempt to utilize any *a priori* knowledge of the underlying physics they demand excessive computing power. Such a Cartesian Maxwell-Fokker-Planck-Landau code has been developed by Ducloux *et al.*¹⁰ and is mostly used for validation purposes.

C. Outline

In this article, we discuss the VFP code OSHUN³² In Secs. II A–II C, we briefly review the algorithms we presented in Tzoufras *et al.*³² Subsequently, in Sec. II D, we present the new implicit method for the electric field, and in Secs. II E–II F the heat-source implementations. Good practices for setting up and diagnosing the simulations are discussed in Secs. III A–III C, and the applicability of the code is demonstrated with two examples in Sec. IV. Finally, in Sec. V, we enumerate the main conclusions from this work.

II. FORMULATION OF THE NUMERICAL SCHEME

The KALOS formalism⁵ was developed to allow VFP codes to model arbitrary momentum distribution functions. In OSHUN we have implemented the full KALOS formalism in 2D3P along with a rigorous collision operator.

A. The KALOS formalism of the Vlasov equation

The KALOS formalism exploits the orthogonality of the spherical harmonics to derive a hierarchy of equations

$$\frac{\partial f_{\ell}^m}{\partial t} - \sum_{\ell'=x,y,z} (A_{\ell,\ell'}^m + B_{\ell,\ell'}^m + E_{\ell,\ell'}^m) = C_{\ell}^m + S_{\ell}^m, \quad (6)$$

where $A_{\ell,\ell'}^m$, $B_{\ell,\ell'}^m$, and $E_{\ell,\ell'}^m$ are expressions for the effects of spatial advection, magnetic fields, and electric fields respectively on the evolution of each amplitude f_{ℓ}^m . These expressions were presented by Bell *et al.*⁵ (Additional terms can be added on the left hand side to accommodate a mixed coordinate frame.²⁵) In formulating a fully explicit algorithm for Eq. (6) we derived a set of operators that describe how each f_{ℓ}^m affects the other amplitudes.³² The algorithm in OSHUN scans the space of spherical harmonics and applies these operators to each f_{ℓ}^m . The computational cost is split between the advection and electric-field operators, with the magnetic field being almost an order of magnitude cheaper. The time-step associated with this fully explicit scheme is limited by the need to resolve plasma waves. In Sec. II D, we present an implicit algorithm for the electric field that removes this constraint by dropping the displacement current.

The first term on the right hand side of Eq. (6) incorporates the effect of collisions. OSHUN utilizes a semi-anisotropic collision operator that has been implemented using a semi-implicit scheme.³² The presence of collisions facilitates the convergence of the spherical harmonic expansion by damping the high-order terms.

A laser pulse can be simulated directly by adding external fields to the left hand side of Eq. (6). This requires that both the laser period and wavelength be resolved. For a laser with wavelength $\lambda_0 = 0.351 \mu\text{m}$ one needs $\Delta x \sim \lambda_0/30 \sim 12 \text{ nm}$ and $\Delta t \sim \lambda_0/(30c) \sim 1.2 \text{ fsec}/30 \sim 0.04 \text{ fsec}$. These

parameters are several orders of magnitude smaller than any other scale of interest in a typical laser-solid interaction. Instead, we can incorporate the macroscopic effect of laser heating by adding external source terms, i.e. S_ℓ^m , to the right hand side of Eq. (6). In this article, we present two such terms, a phenomenological heat source in Sec. II E and an inverse bremsstrahlung source in Sec. II F.

B. Maxwell's equations

In the explicit scheme, we update the electromagnetic fields from Maxwell's equations

$$\frac{\partial \mathbf{B}}{\partial t} = -\nabla \times \mathbf{E}, \quad (7)$$

$$\frac{\partial \mathbf{E}}{\partial t} = \nabla \times \mathbf{B} - \mathbf{J}, \quad (8)$$

where we have adopted the same normalizations as in Tzoufras *et al.*,³² namely, $t \rightarrow \omega_p t$, $\mathbf{r} \rightarrow k_p \mathbf{r}$, $q \rightarrow q/e$, $m \rightarrow m/m_e$, $v \rightarrow v/c$, $n \rightarrow n/n_p$, $\{\mathbf{E}, \mathbf{B}\} \rightarrow e\{\mathbf{E}, \mathbf{B}\}/(m_e c \omega_p)$ where n_p is the plasma density, $\omega_p = \sqrt{4\pi e^2 n_p / m_e}$ the plasma frequency and $k_p^{-1} = c/\omega_p$ the skin depth.

C. The semi-anisotropic Fokker-Planck collision operator

The Fokker-Planck collision operator for a distribution f of particles with mass m and charge $q = ze$ scattering off a distribution F of particles with mass $M = \mu m$ and charge $Q = Ze$ can be written as

$$\frac{1}{\Gamma_{zz}} \left(\frac{\delta f}{\delta t} \right) = \frac{4\pi}{\mu} F f + \left(\frac{\mu-1}{\mu+1} \right) \bar{\nabla} \mathbb{H}(F) \cdot \bar{\nabla} f + \frac{\bar{\nabla} \bar{\nabla} \mathbb{G}(F) : \bar{\nabla} \bar{\nabla} f}{2}, \quad (9)$$

where $\bar{\nabla}$ is the gradient in velocity space, $\Gamma_{zz} = 4\pi(zZe^2)^2 \ln \Lambda / m^2$ and \mathbb{H}, \mathbb{G} the Rosenbluth potentials²⁶ are integral operators for F . This collision operator is fully nonlinear and couples the amplitude of each harmonic to all of the other harmonics.

In Tzoufras *et al.*,³² we linearized Eq. (9) assuming that the distribution functions are weakly anisotropic. Writing the distribution functions F, f as a sum of an isotropic part F_0^0, f_0^0 and an anisotropic perturbation \tilde{F}_a, \tilde{f}_a , $F = F_0^0 + \tilde{F}_a$, $f = f_0^0 + \tilde{f}_a$, Eq. (9) yields

$$\frac{1}{\Gamma_{zz}} \left(\frac{\delta f_0^0}{\delta t} \right) = \frac{4\pi}{\mu} F_0^0 f_0^0 + \left(\frac{\mu-1}{\mu+1} \right) \bar{\nabla} \mathbb{H}(F_0^0) \cdot \bar{\nabla} f_0^0 + \frac{\bar{\nabla} \bar{\nabla} \mathbb{G}(F_0^0) : \bar{\nabla} \bar{\nabla} f_0^0}{2}, \quad (10a)$$

$$\frac{1}{\Gamma_{zz}} \left(\frac{\delta \tilde{f}_a}{\delta t} \right) = \frac{4\pi}{\mu} [F_0^0 \tilde{f}_a + f_0^0 \tilde{F}_a] + \left(\frac{\mu-1}{\mu+1} \right) [\bar{\nabla} \mathbb{H}(F_0^0) \cdot \bar{\nabla} \tilde{f}_a + \bar{\nabla} f_0^0 \cdot \bar{\nabla} \mathbb{H}(\tilde{F}_a)] + \frac{\bar{\nabla} \bar{\nabla} \mathbb{G}(F_0^0) : \bar{\nabla} \bar{\nabla} \tilde{f}_a}{2} + \frac{\bar{\nabla} \bar{\nabla} f_0^0 : \bar{\nabla} \bar{\nabla} \mathbb{G}(\tilde{F}_a)}{2}. \quad (10b)$$

Equation (10a) is nonlinear for the zeroth order amplitudes. On the other hand, Eq. (10b) is linear for the high-order amplitudes. These expressions are valid for any set of species, not just electrons and ions, and enable the development of a multi-species VFP code. OSHUN currently assumes immobile ions, $\mu \rightarrow \infty$, with a density profile determined by Gauss' law. For immobile ions, there are no self-collisions and the electron-ion collision operator reduces to an expression for angular scattering

$$\left(\frac{\delta f_\ell^m}{\delta t} \right)_{e,i,\mu \rightarrow \infty} = -\frac{\ell(\ell+1)}{2} \times \frac{n_i \Gamma_{ei}}{v^3} f_\ell^m. \quad (11)$$

Below we discuss self-collisions, i.e., $F \equiv f$.

1. Isotropic self-collisions

A formulation of the isotropic part of the collision operator that can be discretized in way that conserves the non-relativistic energy and number density integrals was derived by Bobylev and Chuyanov⁷

$$\left(\frac{\delta f_0^0(v)}{\delta t} \right)_{ee} = \frac{4\pi \Gamma_{ee}}{3} \frac{1}{v^2} \frac{\partial}{\partial v} \left[\frac{1}{v} \frac{\partial W(f_0^0(v), v)}{\partial v} \right], \quad (12a)$$

$$W(f_0^0, v) = f_0^0 \int_0^v f_0^0 u^4 du + v^3 f_0^0 \int_v^\infty f_0^0 u du - 3 \int_v^\infty f_0^0 u du \int_0^v f_0^0 u^2 du, \quad (12b)$$

where $(4\pi/3)\Gamma_{ee} \equiv (4\pi/3)4\pi e^4 \ln \Lambda_{ee}/m_e^2$. In Tzoufras *et al.*,³² we normalized time to ω_p^{-1} , velocity to the speed of light c , and the distribution function f to n_e/c^3 , in order to maintain the same dimensionless units as the Vlasov part of the code. However, this normalization is awkward for a non-relativistic collision operator, and yields an expression no more enlightening than Eq. (12) itself. Here, we use the dimensionless units $t = t/\tau_e = \left(\frac{3\sqrt{m}(kT_e)^{3/2}}{4\sqrt{2}\pi n_e e^4 \ln \Lambda} \right)^{-1} t$, $v = v/v_t$, and $f_0^0 = [n_e/(\sqrt{2\pi}v_t)^3]^{-1} f_0^0$. In these units, a Maxwellian distribution with thermal velocity v_t , becomes $f_M(v) = e^{-v^2/2}$. Noting that $[\tau_e n_e/(\sqrt{2\pi}v_t)^3]^{-1} = (4\pi/3)\Gamma_{ee}$ Eq. (12) becomes

$$\left(\frac{\delta f_0^0(v)}{\delta t} \right)_{ee} = \frac{1}{v^2} \frac{\partial}{\partial v} \left[\frac{1}{v} \frac{\partial W(f_0^0(v), v)}{\partial v} \right]. \quad (13)$$

This expression can be discretized directly and shown to conserve $\mathbb{E} = \sum_{n=1}^N (f_0^0)_n v_n^4 \Delta_n$ and $\mathbb{N} = \sum_{n=1}^N (f_0^0)_n v_n^2 \Delta_n$, where $\Delta_n = (v_{n+1} - v_{n-1})/2$.

The cell-size in velocity-space is determined by the need to resolve the coldest distribution in the system. In laser-ablated plasmas, the lowest temperature is usually found in the high-density region of the plasma, where the heat capacity is large and the distribution function nearly Maxwellian. Under these conditions the cell-size is usually chosen $\Delta v \lesssim 0.1 v_{t,\text{cold}} \Rightarrow \Delta v \lesssim 0.1$. If this Δv is sufficient in the beginning of the simulation, $f(v)$ should remain well-resolved thereafter, as the laser raises the temperature of the

plasma. A CFL condition for Eq. (12) can be written as $\Delta t_{\text{CFL}} \propto (\Delta v)^2$. Using a 4th order Runge-Kutta scheme we performed an extensive parameter scan and derived the approximate CFL condition³⁴

$$\Delta t_{\text{iso-FP}} \lesssim 0.3(\Delta v)^2 \iff \Delta t_{\text{iso-FP}} \lesssim 0.3 \left(\frac{\Delta v}{v_t} \right)^2 \tau_e. \quad (14)$$

Although this numerical scheme conserves the non-relativistic integrals \mathbb{E} and \mathbb{N} , it does not conserve the fully relativistic energy and number density integrals. When this operator is used in conjunction with a fully relativistic scheme for the Vlasov description, as is done in OSHUN, energy and—to a lesser degree—density may not be conserved exactly. In laser-ablated plasmas, this can affect the under-dense corona which has low heat capacity and its temperature can be raised by laser irradiation to values above 5 keV.

2. Anisotropic self-collisions

The anisotropic part of the collision operator (10b) yields an expression for each of the amplitudes of the spherical harmonics.³² Including angular scattering and anisotropic self-collisions the expression for f_ℓ^m becomes $\delta f_\ell^m / \delta t = [\mathbf{M}_\ell(f_0^0) - \frac{\ell(\ell+1)}{2} \times \frac{n_e \Gamma_{ei}}{v^3} \mathbf{I}] f_\ell^m$, where the matrices $\mathbf{M}_\ell(f_0^0)$ are linear functions of f_0^0 that depend on ℓ , and \mathbf{I} is the unit matrix. Whereas the isotropic self-collisions are advanced separately by solving equation (10a) we can calculate for each ℓ the matrix $\mathbf{M}_\ell(f_0^{0,[n+1]})$ to develop the implicit scheme

$$f_\ell^{m,[n+1]} = \left[\left(1 + \frac{\ell(\ell+1)}{2} \frac{n_e \Gamma_{ei} \Delta t}{v^3} \right) \mathbf{I} - \Delta t \mathbf{M}_\ell^{[n+1]} \right]^{-1} f_\ell^{m,[n]}, \quad (15)$$

where $\mathbf{M}_\ell^{[n+1]}$ denotes $\mathbf{M}_\ell(f_0^{0,[n+1]})$. Because $\mathbf{M}_\ell^{[n+1]}$ does not depend on the m index, only ℓ matrices need to be inverted. Finally we note that if the determinant of $(1 + \frac{\ell(\ell+1)}{2} \frac{n_e \Gamma_{ei} \Delta t}{v^3}) \mathbf{I} - \Delta t \mathbf{M}_\ell^{[n+1]}$ vanishes this indicates that Δt is too large to yield realistic results. $\Delta t \lesssim \tau_{ei}$ is necessary to ensure accurate modeling of electron transport.

D. Implicit solver for the electric field

Collisions in dense plasmas tend to damp high-frequency waves. It is therefore common to drop the displacement current from Ampère's law, i.e., $\mathbf{J} \simeq \nabla \times \mathbf{B}$, to avoid having to resolve inconsequential high-frequency phenomena including electromagnetic and plasma waves. Moreover, in such plasmas, the conservation of charge guarantees quasi-neutrality $\nabla \cdot \mathbf{J} = 0 \iff \partial_t \rho = 0$. For the numerical scheme, this means that Ampère's law becomes an expression for updating the current, as opposed to the electric field

$$\left(\frac{\partial \mathbf{B}}{\partial t} = -\nabla \times \mathbf{E}^{[n]} \right) \rightarrow \mathbf{B}^{[n+1]}, \quad (16a)$$

$$\mathbf{J}^{[n+1]} = \nabla \times \mathbf{B}^{[n+1]}. \quad (16b)$$

A separate expression is then required to update the electric field. The fact that Eq. (16a) must be satisfied by the distribution function can be used to predict the electric field $\mathbf{E}^{[n+1]}$

$$\varepsilon_{ijk} \nabla_j \mathbf{B}_k^{[n+1]} = \mathbf{J}_i^{[n+1]} = \mathbf{J}_i^{[n+1]}(0) + \frac{\delta J_i(\delta E_j)}{\delta E_j} \cdot \mathbf{E}_j^{[n+1]}, \quad (17)$$

where $\mathbf{J}_i^{[n+1]}(0)$ is the current in the absence of an electric field, $\frac{\delta J_i}{\delta E_j}$ a “conductivity” tensor which shows the effect of electric field perturbations δE_j on the current δJ_i , and $\mathbf{E}_j^{[n+1]}$ to be determined.³⁵ Before discussing how Eq. (17) is to be treated we remind that the current is directly connected to the first order spherical harmonics

$$\mathbf{J}_x = -\frac{4\pi}{3} \int_0^\infty dp \frac{p^3}{\gamma} f_1^0, \quad (18a)$$

$$\mathbf{J}_y + i\mathbf{J}_z = -\frac{8\pi}{3} \int_0^\infty dp \frac{p^3}{\gamma} \{ \Re[f_1^1] - i\Im[f_1^1] \}. \quad (18b)$$

To calculate $\mathbf{J}_i^{[n+1]}(0)$ we first complete the explicit part of the calculation with $\mathbf{E} = 0$. This includes the effect of the magnetic field and spatial advection on f , the collisions for the isotropic part of f , and the heat source (if any). We denote the resulting value of f as $f^{[n+1],\text{expl}}$, where the “ \star ” symbol indicates that the effect of the electric field on f has been omitted. We then apply the anisotropic part of the collision operator to f_1^0 and f_1^1 to obtain $(f_1^0)^{[n+1]}(0)$, $(f_1^1)^{[n+1]}(0)$, and therefore $\mathbf{J}^{[n+1]}(0)$ from Eqs. (18).

For the conductivity tensor, we start from $f^{[n+1],\text{expl}}$ and find the plasma response to three perturbations $\delta E_i \hat{e}_i$, $i = x, y, z$. The electric field operators (expressions (A1)–(A8) in Tzoufras *et al.*³²) do not need to be applied to all of the harmonics, just those that affect the values of $(f_1^0)^{[n+1]}$ and $(f_1^1)^{[n+1]}$. For a second order method, e.g., RK2, these calculations will involve harmonics with $\ell \leq 3$ for the first sub-step and $\ell \leq 2$ for the second. A map of the operator applications for a second order scheme is presented in Fig. 1. For $\delta E_x \hat{e}_x$ we need to perform the operations on the top row and then use the anisotropic part of the collision operator on f_1^0 and f_1^1 to obtain $\mathbf{J}^{[n+1]}(\delta E_x \hat{e}_x)$. The process is repeated for $\delta E_i \hat{e}_i$, $i = y, z$ to obtain $\mathbf{J}^{[n+1]}(\delta E_y \hat{e}_y)$ and $\mathbf{J}^{[n+1]}(\delta E_z \hat{e}_z)$. Substitution of the resulting tensor $\delta J_i / \delta E_j$ into Eq. (17) yields

$$\varepsilon_{ijk} \nabla_j \mathbf{B}_k^{[n+1]} = \mathbf{J}_i^{[n+1]}(0) + \frac{\mathbf{J}_i^{[n+1]}(\delta E_j) - \mathbf{J}_i^{[n+1]}(0)}{\delta E_j} \mathbf{E}_j^{[n+1]}. \quad (19)$$

This is a 3×3 system of equations for $\mathbf{E}^{[n+1]}$. The final steps are to use this electric field to update the entire distribution function and then apply the anisotropic part of the collision operator.

This algorithm imposes negligible computational cost, and because it drops high-frequency waves it allows for large time-steps to be taken. We typically choose the time-step on the order of the collision time. In OSHUN the user can decide between this scheme and the algorithm described in Secs. II A–II C in the input file.

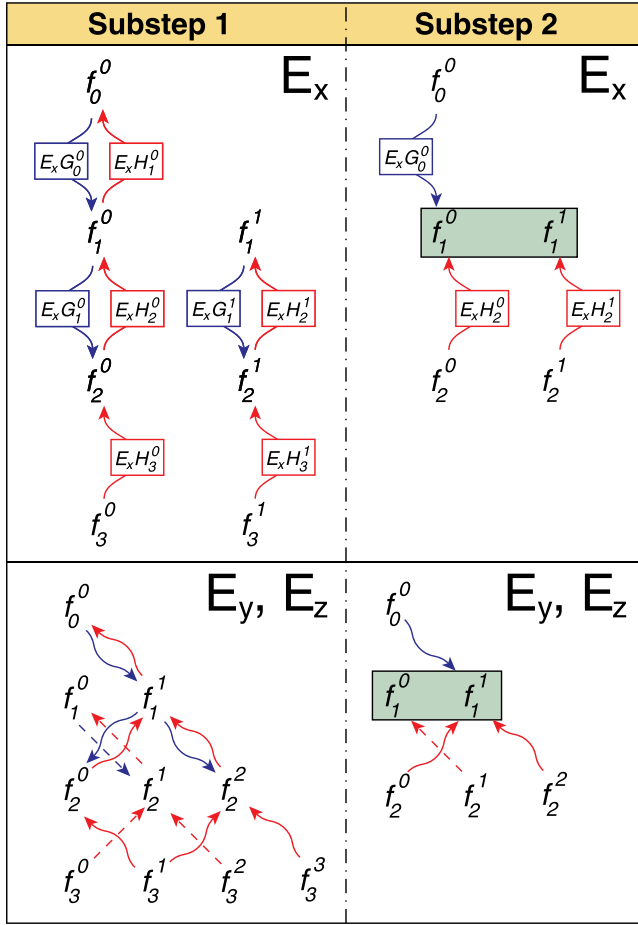


FIG. 1. A map of the operations necessary to calculate the effect of $\delta E_i \hat{e}_i$, $i = x, y, z$ on the current in a second order scheme. The top row shows the algorithm for $\delta E_x \hat{e}_x$, which requires a total of 11 operations. The bottom row is for $\delta E_y \hat{e}_y$ or $\delta E_z \hat{e}_z$ and it requires a total of 17 operations.

E. Phenomenological laser source

To incorporate a phenomenological laser source we assume that a portion $0 \leq \alpha < 1$ of the distribution function $f(t)$ is converted to a new “hot” distribution in a time interval Δt , i.e., $f(t + \Delta t) = \alpha f_{hot}(t) + (1 - \alpha)f(t)$, where the distribution $f_{hot}(t)$ can be specified by the user. The temperature rise is then expressed as $\Delta T = T(t + \Delta t) - T(t) = \alpha [T_{hot}(t) - T(t)]$. For a specified heat-source profile, the deposition of energy ΔE_i in each cell “ i ” causes a temperature rise equal to $\Delta T_i = \Delta E_i / (n_i V_i)$, where n_i is the local density and V_i the cell volume. This yields the local value for $\alpha_i = \Delta E_i / [n_i V_i (T_{hot,i}(t) - T_i(t))]$. We usually assume that $f_{hot}(t)$ is a Maxwellian with temperature determined from the local laser intensity.

F. Inverse bremsstrahlung operator

The inverse bremsstrahlung source associated with a dipole electric field $E(t) = E_0 \cos(\omega_0 t)$ can be written as¹⁹

$$\frac{\partial f_0^0(v)}{\partial t} = \frac{A}{3} \left(\frac{v_{os}}{v} \right)^2 \frac{\partial}{\partial v} \left(\frac{g(v)}{v} \frac{\partial f_0^0(v)}{\partial v} \right), \quad (20)$$

where $g(v) = [1 + (v_{\omega}/v)^6]^{-1}$, $A = 2\pi n_i Z^2 \frac{e^4}{m_e^2} \log \Lambda_{ei}$, $v_{os} = eE_0 / (m_e \omega_0)$, and the coefficient v_{ω} is determined from the

expression $v_{ei}(v_{\omega}) = A/v_{\omega}^3 = \omega_0/2$. To simplify Eq. (20), we assume a quasi-neutral plasma $n_e \simeq Z n_i$ and $\log \Lambda_{ei} \simeq \log \Lambda_{ee}$. Using dimensionless velocity $v = v/v_t$ (and $v_{os} = v_{os}/v_t$) and time $t = t/\tau_e$, and substituting $A = 3v_t^3 (\sqrt{\pi}/8) (Z/\tau_e)$ into Eq. (20) we obtain

$$\frac{\partial f_0^0(v)}{\partial t} \simeq \sqrt{\frac{\pi}{8}} Z v_{os}^2 \frac{1}{v^2} \frac{\partial}{\partial v} \left(\frac{g(v)}{v} \frac{\partial f_0^0(v)}{\partial v} \right). \quad (21)$$

Equation (20) may be discretized in the same way as expression (13) for the self-collision operator, and we have incorporated such an explicit inverse bremsstrahlung source into OSHUN.

In Fig. 2, we show the benchmark of the inverse bremsstrahlung operator against an external dipole electric field; to our knowledge this is the first such comparison. We initialize a Maxwellian plasma with thermal velocity $v_t = 0.04421c$, that is $T_e \simeq 1$ keV, density $n_e = 1.5 \times 10^{21} \text{ cm}^{-3}$ and $Z = 12$. The distribution function at initialization is shown with a solid black line. A laser with intensity $I = 6.95 \times 10^{15} \text{ W/cm}^2$ and wavelength $\lambda_0 = 0.351 \mu\text{m}$ is assumed, such that $v_{os} \simeq 0.025c \simeq 0.57v_t$. For these parameters, we performed a simulation with an external electric field $E = E_0 \cos(\omega_0 t) \hat{e}_y$, where $(\ell_0, m_0) = (3, 2)$ and $\Delta t = 0.0123 \omega_0^{-1}$, and the resulting electron distribution function after 2.666 ps is shown in Fig. 2 with the dotted red line. We repeated the simulation using the inverse bremsstrahlung operator instead of the external dipole field and the new distribution after 2.666 ps is shown with the broken blue line. Both of these approaches recover the flat-top shape near the origin and the sharp fall-off at large velocities predicted by Langdon¹⁹ and they are in excellent agreement with each other.

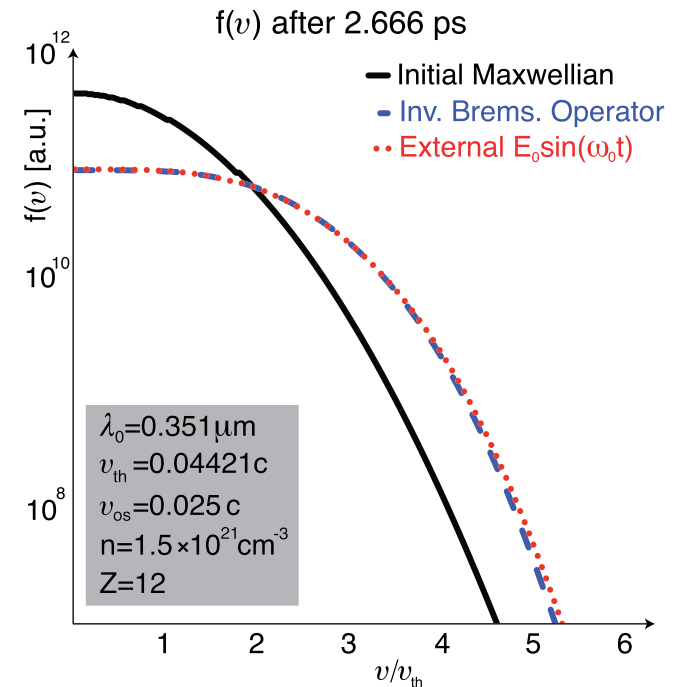


FIG. 2. An initial Maxwellian plasma (solid black line) heated by the inverse bremsstrahlung operator (broken blue line) or a dipole electric field (dotted red line). The inverse bremsstrahlung operator recovers the shape of the DLM^{11,12,19,23} distribution function calculated using a dipole electric field.

III. DIAGNOSING NUMERICAL ARTIFACTS AND EXTRACTING PHYSICS FROM VFP SIMULATIONS

A. 1D2P simulations

The most glaring failures of a numerical scheme for simulating HEDLP are those accompanied by unphysical moments of the distribution function, for example, when the plasma density or the temperature become negative. Unfortunately, numerical artifacts originating from an inconsiderate truncation of the spherical harmonic expansion do not always manifest themselves so blatantly, because most quantities of interest are associated with the isotropic zeroth-order harmonic that is only indirectly affected by the truncation. Furthermore, to establish the validity of a kinetic code, we must examine kinetic information, namely, distribution functions or particle trajectories; integrals over the particle distribution can obscure underlying unphysical structures. Here, we present such a convergence study for a 1D2P non-local transport problem under conditions similar to those found in ICF *Hohlraums*.

We consider a 1D system, $0 \leq x[\text{cm}] \leq 1$, with initial temperature 1 keV, $Z = 4$, and constant density $5 \times 10^{20} \text{ cm}^{-3}$. The plasma is heated by an inverse bremsstrahlung source corresponding to a laser with intensity profile $I = 10^{16} e^{-0.5[x/(1.21\text{mm})]^2} \text{ W/cm}^2$ and wavelength $\lambda_0 = 0.33 \mu\text{m}$, such that $Z \times v_{os}^2 \simeq 1.0$. The heating profile is constant in time, the boundaries are reflecting, and the implicit algorithm is used for the electric field. This allows us to choose a timestep $\Delta t = 30\omega_p^{-1} \simeq \tau_{ei}/32 \simeq 24\text{fs}$. The simulation is terminated after 200 ps at which time the maximum temperature in the simulation domain is about 5 keV. The maximum magnitude of momentum in the p-mesh is set to $p_{\text{max}} = 0.6m_e c$, such that a plasma with temperature 5 keV and thermal velocity $v_{t,5\text{keV}} \simeq 0.1c$ can be accommodated. The total number of mesh-points in p-space is 432 to ensure that the coldest distribution, the initial Maxwellian with $v_{t,1\text{keV}} = 0.4421$, is finely resolved with $30\Delta v < v_{t,1\text{keV}}$.

In Fig. 3, we show the projection of the distribution function onto Cartesian phase-space after 200 ps, i.e. $f(p_x, x, 200\text{ps}) = \int_{-\infty}^{\infty} \int_{-\infty}^{\infty} f(\mathbf{p}, x, 200\text{ps}) dp_y dp_z$, from four simulations using: the diffusive approximation, 4 harmonics, 8 harmonics, and 32 harmonics. The color bars show the amplitude of $f(p_x, x, 200\text{ps})$ in logarithmic scales. For

positive/negative values of $f(p_x, x, 200\text{ps})$ we use the orange/blue color-scale. The maximum value for the blue color-scale is reduced from panel to panel to allow us to discern negative values for $f(p_x, x, 200\text{ps})$ as the number of harmonics increases. In principle $f(p_x, x, 200\text{ps})$ should be positive definite, negative values are numerical artifacts. We note that these negative values are merely projections of the distribution produced by data post-processing, they are not used in the code which only cares for spherical harmonics.

During the simulation, the plasma is heated on the left side of the box and multi-keV particles start streaming across the simulation domain generating non-Maxwellian tails for $p_x > 0$. The plasma self-consistently generates a return-current to maintain charge neutrality. In the first panel on the left in Fig. 3 we plot the distribution function from a simulation using the diffusive approximation. Negative values are prevalent throughout the simulation for $p_x \leq -0.2m_e c$. For momenta $|p_x| < 0.2m_e c$ the diffusive approximation seems sufficient. For $|p_x| > 0.2m_e c$ angular scattering is not strong enough to damp the high-order harmonics and the electron distribution exhibits negative values. (For positive momenta, the presence of the non-local electrons masks any artifacts of the background population.) When we increase the number of harmonics to 4, see second panel from the left, we notice that the negative values show up for $p_x \leq -0.27m_e c$ and they are two orders of magnitude smaller. Increasing the number of terms in the expansion to 8, and then to 32, we observe that the negative values continue to shift farther out in the tail of the distribution and their absolute values become vanishingly small. In the last plot, for $\ell_0 = 31$, the errors due to the truncation are negligible, compared, for example, with the errors due to the usage of a non-relativistic collision operator, and we can safely argue that the expansion has converged.

Another way of tracking the accuracy of the diffusive approximation, is to monitor the ratio of $f_1^0(p)/f_0^0(p)$ and report instances of $f_1^0(p)/f_0^0(p) \sim 1$. However, unless there is a mitigation strategy, or at least a way of finding out how the lack of convergence at $p \gg p_t$ affects the physics at lower momenta, the usefulness of this approach is going to be limited. Full convergence studies are advisable unless $f_1^0(p)/f_0^0(p) \ll 1, \forall p$.

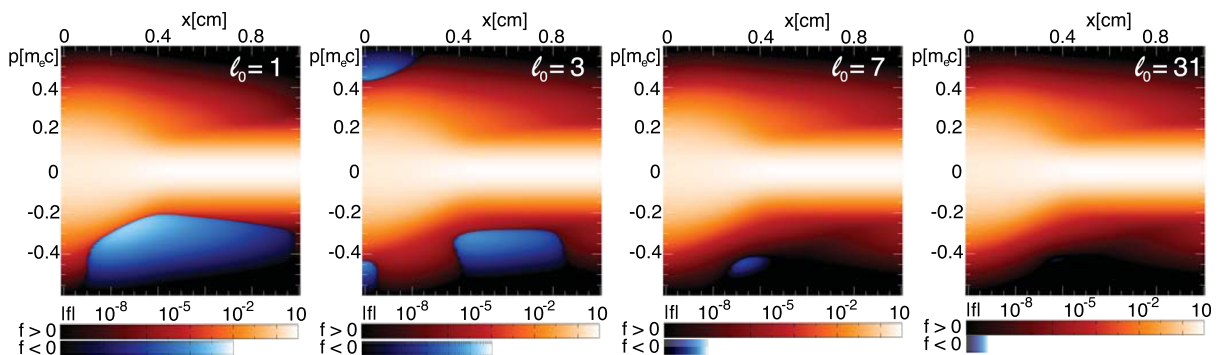


FIG. 3. Four non-local transport simulations using different numbers of spherical harmonics and projected onto a Cartesian mesh. A plasma with density $5 \times 10^{20} \text{ cm}^{-3}$, $Z = 4$, and initial temperature 1 keV is heated from the left with an inverse bremsstrahlung source with profile $I = 10^{16} e^{-0.5[x/(1.21\text{mm})]^2} \text{ W/cm}^2$ and $\lambda_0 = 0.33 \mu\text{m}$. This set of simulations shows that convergence can be achieved when sufficient number of spherical harmonics is used.

B. 2D3P simulations

To describe the three-dimensional p -space two indices ($\ell \leq \ell_0, m \leq m_0 \leq \ell_0$) are needed, as opposed to just one ($\ell \leq \ell_0$) for 1D2P simulations. In Tzoufras *et al.*,³² we argued that $m_0 < \ell_0$ may often be used with no apparent difference in the physics. (In particular we showed that the structure of the current filaments in the early non-linear stage of the electromagnetic instability were virtually identical for simulations with $\ell_0 = 48$ and $3 \leq m_0 \leq 48$.) We have observed that using $m_0 < \ell_0$ also works well for many laser-irradiated plasmas. However, if either ℓ_0 or m_0 is set to values much lower than those required for convergence the code can produce strikingly artificial structures. Paradoxically the diffusive approximation, with $m_0 = \ell_0 = 1$, is the least prone to such artifacts and diffusive simulations tend to run rapidly and stably generating seemingly plausible results. This insidious feature of the diffusive approximation is likely due to the fact that $m_0 = \ell_0 = 1$ precludes anisotropic pressure and temperature from building up and driving numerical instabilities, such that would expose the need for a more careful treatment.

C. The current-filamentation instability as a numerical artifact

The growth of the current-filamentation instability³³ from numerical noise is one of the biggest challenges for multi-dimensional simulations with OSHUN. This instability grows whenever there is anisotropy in the particle distribution function and it is associated with a feedback mechanism between magnetic fields and current filaments.¹⁴ Its manifestation can vary depending on the degree of anisotropy in the distribution function⁹ and the level of collisionality.²⁴ For modes with long wavelength the growth rate reduces—but remains non-zero—with the wavenumber of the perturbation, $\gamma \sim O(k)$. The maximum growth rate of the instability occurs at much shorter wavelengths.^{9,24,31}

In VFP codes, there is no natural noise for instabilities to grow from. To study instabilities, one must provide suitable well-resolved perturbations, otherwise, they may grow from the only source of noise in the system, that is, the numerical mesh. In multi-dimensional VFP simulations, we typically choose cell-sizes several orders of magnitude larger than the natural wavelength for the current-filamentation instability, i.e., $\Delta x \gg O(c/\omega_p)$. As a result, the fastest-growing mode supported by the mesh has filaments with width equal to the cell-size. The presence of the instability is then correctly predicted by the code, but neither its growth rate nor its wavelength is physical.

In Sec. IV B, we consider the interaction of a moderate-intensity ($\sim 10^{16}$ W/cm²) laser with an inhomogeneous plasma with density ranging from underdense to solid. PIC simulations show that the absorption is dominated by parametric instabilities and there is no evidence of the current-filamentation instability even though the resulting electron distribution in the underdense region is anisotropic. In order to model non-local heat conduction for realistic temporal and spatial scales, we ignore the microphysics of the parametric instabilities and use OSHUN with an external heat source that describes the macroscopic effect of laser heating.

However, an unintended consequence of dropping these competing phenomena, is that the current-filamentation instability can grow from numerical noise in the underdense plasma. In this scenario, we may need to look for ways of suppressing this instability.

The most straightforward solution is to perform electrostatic simulations. This may be sufficient in problems where no significant magnetic fields arise. Alternatively, the diffusive approximation allows us to use magnetic fields and suppresses the instability by prohibiting temperature/pressure anisotropy. Another option, one that facilitates both magnetic fields and a detailed description of the particle distribution, is to use very coarse resolution in configuration-space to reduce the growth of the instability enough that it remains effectively suppressed for the entire simulation. This approach was used in Sec. IV B.

IV. EXAMPLES

A. A physical picture for flux-limited heat conduction

For a time-independent sinusoidal temperature perturbation $T(x) = T_0 + T_1 \sin(kx)$, with $T_1 \ll T_0$, the corresponding heat flux is¹ $Q(x) = Q_1 \sin(kx + \pi/2)$. A general temperature profile $T(x) = T_0 + \tilde{T}_1(x)$ may then be decomposed into harmonic functions with amplitude $\hat{T}(k)$ which result in a heat flux with magnitude $\hat{Q}(k)$. An effective heat conduction coefficient $\hat{\kappa}(k)$ can be defined such that $\hat{Q}(k) = -ik\hat{\kappa}(k)\hat{T}(k)$. The inverse Fourier transform of this expression yields a convolution integral for heat conduction $Q(x) = -\int_{-\infty}^{\infty} ik\hat{\kappa}(k)\hat{T}(k)e^{ikx}dk = -\int_{-\infty}^{\infty} G(x-x')\nabla\tilde{T}_1(x')dx'$, where $G(x) = \int_{-\infty}^{\infty} \hat{\kappa}(k)e^{ikx}dk$. The challenge is finding an expression for the kernel $G(x)$ or equivalently for the effective heat conduction coefficient $\hat{\kappa}(k)$. Epperlein and Short¹³ performed a series of VFP simulations for high-Z materials with 1D sinusoidal perturbations $\tilde{T}_1(x) = T_1 \sin(k_i x)$ to obtain the values for $\hat{\kappa}(k_i)$. Here, we repeat these tests using OSHUN with the explicit electric-field solver for $Z = 1$. A more detailed discussion including higher Z was recently presented by A. Marocchino *et al.*²¹

We initialize a homogeneous plasma with density 10^{23} cm⁻³ and a sinusoidal temperature profile $T[\text{eV}] = 307 \text{ eV} + 12.5 \text{ eV} \times \sin(k_i x)$ in a 1D periodic box with size $L_i = 2\pi/k_i$. The maximum box size for this parameter scan is $L_1 = 1000\lambda_e$, where the mean free path is $\lambda_e = v_i\tau_e$. The simulation time is $\tau_S = 40\tau_e$ to allow particles at the tail of the distribution with velocity $v \sim 3v_i$ to undergo 90° scattering. The p -space was resolved with 108 cells and $p_{\text{max}} = 0.15m_e c \simeq 6m_e v_i$. Sufficient spherical harmonics are kept in the expansion to accurately capture the angular profile of the distribution function.

Quoting a single number for the effective heat conduction coefficient from each simulation suggests the existence of a steady state. For a smooth temperature profile, $L_i \gg \lambda_e$, the ratio $Q(x)/\nabla T_e(x)$ reaches steady state after about $20\tau_e$ and is nearly constant throughout the simulation box. The effective heat conduction coefficient may then be measured unambiguously. For the highly non-local cases (i.e., those with short perturbation wavelength) a steady state is established more quickly, as hot electrons decouple from the background and travel many times around the box sharing

their energy with the entire plasma and causing rapid dissipation of the temperature perturbation. In all cases, the ratio $Q(x)/\nabla T_e(x)$ is measured at steady state, when its value becomes constant across the simulation box. The parameter scan has been repeated for different types of perturbations, and the results are identical once a steady state is established. This confirms that the effective heat conduction coefficient only depends on the wavelength of the perturbation normalized to the mean free path.

The ratio of the effective heat conduction coefficient $\hat{\kappa}(k_i)$ from VFP simulations to the Spitzer and H rm value $\kappa_{SH} = 3.20$ is shown with red squares in Figure 4. This ratio can be viewed as a “flux limiter” $f(k_i) = \hat{\kappa}(k_i)/\kappa_{SH}$. The longitudinal axis is the temperature wavenumber normalized to the mean free path $\lambda_e(\langle T_e \rangle)$. For long wavelengths most of the electrons transfer their energy locally, and $f \sim 1$. As the wavenumber increases, the hot electrons decouple from the system and belong collectively to the entire simulation box, rather than any one location. Fewer electrons are then available to transfer energy locally, and those that do have less energy to carry. This causes an apparent reduction in the local heat flux which is captured by the drop in the ratio $\hat{\kappa}(k_i)/\kappa_{SH}$.

To derive an analytical estimate based on this physical picture we consider an electron moving with velocity $v_c = \alpha v_t$. The time it takes for this electron to undergo 90° scattering is $\tau_c = \alpha^3 \tau_e$ and the distance it travels is $v_c \tau_c = \alpha^4 \lambda_e$. If the mean free path $v_c \tau_c$ exceeds the “de-coupling” length the contribution of this electron to the heat flux can be ignored. This de-coupling length is the distance that must be traveled to ensure that ∇T switches sign. For a sinusoidal temperature profile, this distance is equal to half the wavelength of the perturbation, i.e., $\pi/k = \alpha^4 \lambda_e \Rightarrow v_c = (k \lambda_e / \pi)^{-1/4} v_t$. Electrons with initial velocities $|v_x| > v_c$ form a “superfluid” that belongs collectively to the entire system and does not contribute to the local heat flux.

In a Maxwellian plasma, the heat flux of the electrons with velocity $|v_x| > v_c$ is $\langle v^2 |v_x| \rangle_{|v_x| > v_c} = \frac{4\sqrt{2}}{\sqrt{\pi}} v_t^3 \left(\frac{v_c^2}{4v_t^2} + 1 \right) e^{-v_c^2/(2v_t^2)}$. The ratio of the effective heat conduction

coefficient to κ_{SH} becomes $f = 1 - \frac{\langle v^2 |v_x| \rangle_{|v_x| > v_c}}{\langle v^2 |v_x| \rangle_{|v_x| > 0}}$. From the discussion above, we can substitute the velocity v_c in the expression for the heat flux to obtain

$$\frac{\hat{\kappa}(k)}{\kappa_{SH}} \sim 1 - \left(1 + \frac{1}{4} \sqrt{\frac{\pi}{k \lambda_e}} \right) e^{-\frac{1}{2} \sqrt{\frac{\pi}{k \lambda_e}}}. \quad (22)$$

The ratio $\hat{\kappa}/\kappa_{SH}$ from Eq. (22) is shown in Figure 4 and agrees well with the detailed VFP calculations for $k \lambda_e \ll 1$.

B. Asymmetric heating of a solid-density target

One of the main motivations for developing OSHUN is to model multi-dimensional non-local transport in laser-irradiated plasmas. Here, we present an example of such a simulation, part of a study we have undertaken to understand how asymmetry in the irradiation pattern affects the pressure profile in dense targets. At present ion motion has not been incorporated into the code and simulation times must be relatively limited.

We consider a planar target with constant temperature 500 eV, $Z = 4$, and a sharp density gradient rising from 10^{21} cm^{-3} to 10^{23} cm^{-3} within about $30 \mu\text{m}$. The exact density profile is replicated on top of each of the plots in Figure 5. A phenomenological heat source is introduced with intensity profile $I = 10^{16} e^{-\frac{y^2}{2 \times (250 \mu\text{m})^2}} \times [1 - (1 - \frac{t}{10 \text{ ps}}) H(1 - \frac{t}{10 \text{ ps}})] \frac{\text{W}}{\text{cm}^2}$, where $H(x) = \int_{-\infty}^x \delta(t) dt$ is the Heaviside step function. We assume that the laser energy is deposited in the low-density region—as one might expect from laser-plasma instabilities—

with a Gaussian profile $e^{-\frac{(x+180 \mu\text{m})^2}{(120 \mu\text{m})^2}}$. The “hot” Maxwellian distribution has temperature $T_{\text{hot}} = T_e + \sqrt{\frac{I}{10^{14} \text{ W/cm}^2 \mu\text{m}}} \frac{\lambda_0}{\mu\text{m}} \text{ keV}$, where I is the heat source intensity and $\lambda_0 = 0.351 \mu\text{m}$. The simulation employs the implicit solver for the electric field presented in Sec. II D. The system is resolved with $\Delta x = 7.3 \mu\text{m}$ and $\Delta y = 31.25 \mu\text{m}$, where the resolution in x is set by the need to resolve the density gradient and in y to resolve the structure of the heat source and its imprint on the plasma. 300 cells are used for the magnitude of momentum with $p_{\text{max}} = 0.6 m_e c$, and $(\ell_0, m_0) = (16, 4)$, that is 75 terms in the harmonic expansion. The implicit time-step was set to $\Delta t_{\text{impl}} \simeq 0.65 \tau_{ei, 0.5 \text{ keV}} \simeq 1.68 \text{ fs}$.

The pressure and temperature profiles, as well as the longitudinal electric (E_x) and transverse magnetic (B_z) fields are shown in Figure 5 after 10 ps (top row) and 20 ps (bottom row). (The results in the bottom row have been reflected to facilitate comparison with those on the top row.) A detailed discussion of the physics requires further analysis and additional simulations; here we briefly point out the salient features of the interaction.

A heat-front develops in the under-dense corona and starts climbing the sharp density gradient. Pressure builds on the gradient reaching 110 Mbar at the end of the simulation. Meanwhile, non-local electrons travel in the solid-density plasma (up to $100 \mu\text{m}$) and lead to a measurable change in both temperature and pressure. The sharp density gradient generates an electric field $E_x = -\nabla P/e$. Transversely

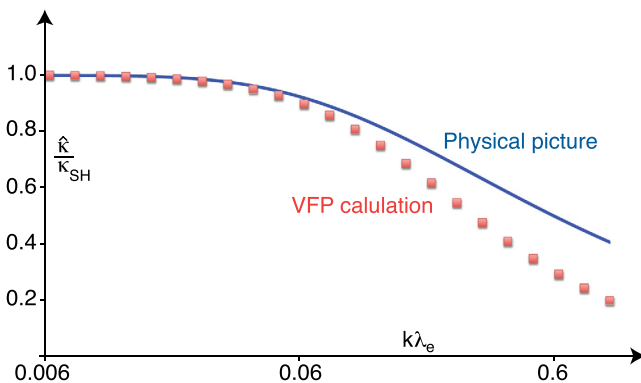


FIG. 4. The ratio of the effective heat conduction coefficient from VFP simulations to the Spitzer and H rm value, $f = \hat{\kappa}(k_i)/\kappa_{SH}$, is shown with red squares as a function of the wavenumber of the temperature perturbation. We have also overlaid a blue solid line that corresponds to expression (22) in the text. Good agreement between the VFP results and expression (22) is observed for $k \lambda_e \ll 1$.

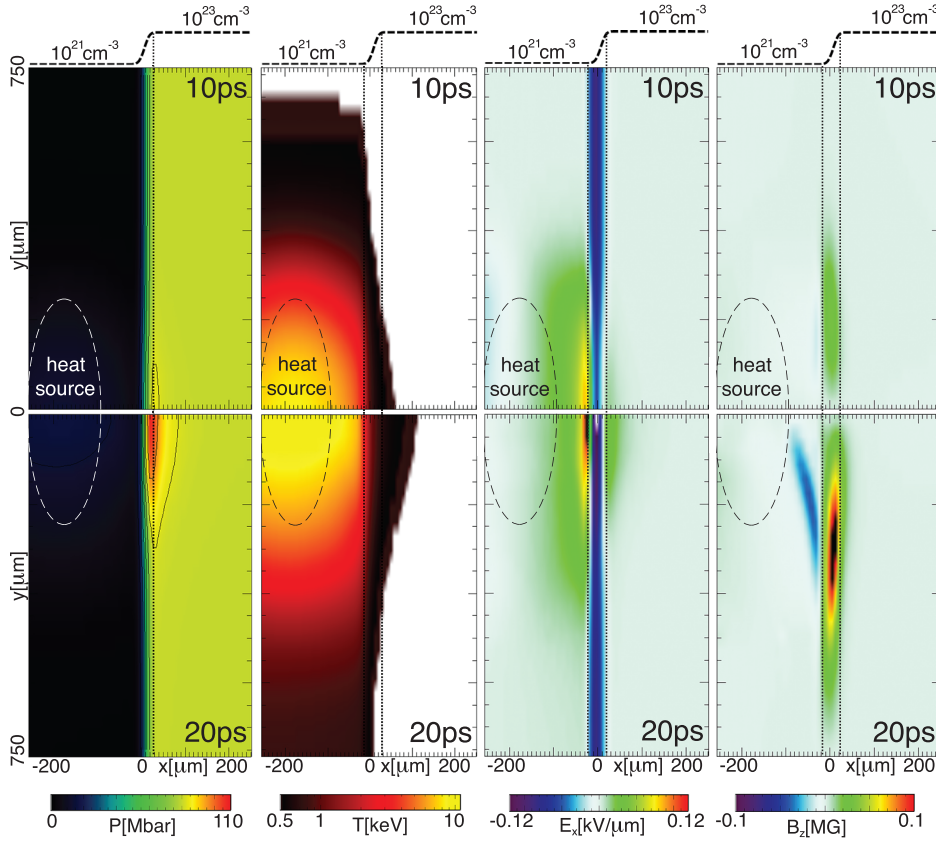


FIG. 5. The corona of a planar solid-density target is heated by a source with intensity

$$I = 10^{16} e^{-\frac{y^2}{2 \times (250 \mu\text{m})^2}} \times \left[1 - \left(1 - \frac{t}{10 \text{ ps}} \right) H \left(1 - \frac{t}{10 \text{ ps}} \right) \right] \frac{\text{W}}{\text{cm}^2}.$$

The pressure and temperature profiles, as well as the longitudinal electric (E_x) and transverse magnetic (B_z) fields are shown after 10 ps and 20 ps.

asymmetric heating on this gradient can be expected to generate an electric field with maximum magnitude on axis, thereby driving a magnetic field (due to the Biermann battery). However, here the situation is more complex. The heat source resides in a region with constant density, and early in time the gradient is heated by non-local electrons which are accompanied by a resistive electric field. This field has the opposite sign from the one due to ∇P . From Figure 5, we see that $|E_x(10\text{ps})|$ is smaller on-axis in the region between the dotted lines, where $\nabla n \neq 0$. At the same time, resistive electric fields are visible both to the left and right of the gradient. At 20 ps the heat front has reached the region between the dotted lines and $|E_x(20\text{ps})|$ is maximum on axis. The resistive electric field in the solid density material at 20 ps is also more prominent. The evolution of the electric field leads to the large changes observed in the B_z structure from 10 ps to 20 ps. It is conceivable that for systems with higher peak density and longer irradiation time B_z on the surface of the target is strong enough to magnetize the plasma. The relative importance of the underlying phenomena depends on the density and heat-source profiles.

V. CONCLUSIONS

We have developed the VFP code OSHUN to study High Energy Density Laboratory Plasmas. OSHUN employs the spherical harmonic expansion in momentum-space to facilitate the description of arbitrarily anisotropic distribution functions in the presence of collisions. It implements the KALOS hierarchy of equations⁵ for the effects of spatial advection, electric and magnetic fields, and incorporates a

rigorous semi-anisotropic Fokker-Planck collision operator. The code is currently being used for a number of studies relevant to Inertial Fusion Energy (IFE), which have motivated further advances in the numerical scheme and have allowed us to assess the potential and the limitations of OSHUN

- (1) An implicit algorithm for the electric field has been developed. Its computational cost is nearly the same as that of the explicit algorithm in Tzoufras *et al.*,³² but it allows us to circumvent the CFL condition(s) due to high-frequency waves, thereby enabling *nsec*-scale electron transport simulations.
- (2) An inverse bremsstrahlung source has been implemented and shown to recover the DLM distribution functions. Benchmarks against simulations with a dipole electric field yield excellent agreement.
- (3) A careful convergence study is always required to justify the truncation of the spherical harmonic expansion. Otherwise it is difficult to identify whether the simulation results are physical or numerical artifacts.
- (4) Non-local transport leads to anisotropic particle distributions which are susceptible to the current-filamentation instability. Although VFP codes are noiseless, the instability can still grow from numerical noise. We can avoid this by carefully choosing the simulation parameters.
- (5) Non-local transport can be simulated for realistic IFE target geometries and time-scales. To perform such simulations we must incorporate mobile ions. This can be done either by modeling the ions as a fluid or adding them as a separate distribution function. Both approaches will be pursued.

ACKNOWLEDGMENTS

We acknowledge support by the DOE under Fusion Science Center through a University of Rochester Subcontract No. 415025-G and under DE-FG52-09NA29552 and DE-NA0001833. Simulations were performed at the Hoffman2 cluster in UCLA. We also acknowledge useful discussions with Dr. B. Reville.

- ¹A. R. Bell, "Transport in laser-produced plasmas," In *proceedings of the Forty Fifth Scottish Universities Summer School in Physics, St. Andrews* (1995), pp. 138–167.
- ²A. R. Bell, "Electron energy transport in ion waves and its relevance to laser-produced plasmas," *Phys. Fluids* **26**(1), 279–284 (1983).
- ³A. R. Bell and M. Tzoufras, "Electron transport and shock ignition," *Plasma Phys. Controlled Fusion* **53**(4), 045010 (2011).
- ⁴A. R. Bell, R. G. Evans, and D. J. Nicholas, "Electron energy transport in steep temperature gradients in laser-produced plasmas," *Phys. Rev. Lett.* **46**(4), 243–246 (1981).
- ⁵A. R. Bell, A. P. L. Robinson, M. Sherlock, R. J. Kingham, and W. Rozmus, "Fast electron transport in laser-produced plasmas and the Kalos code for solution of the Vlasov–Fokker–Planck equation," *Plasma Phys. Controlled Fusion* **48**(3), R37–R57 (2006).
- ⁶A. R. Bell, K. M. Schure, and B. Reville, "Cosmic ray acceleration at oblique shocks," *Mon. Not. R. Astron. Soc.* **418**(2), 1208–1216 (2011).
- ⁷A. V. Bobylev and V. A. Chuyanov, "On the numerical solution of Landau's kinetic equation," *USSR Comput. Math. Math. Phys.* **16**(2), 121–130 (1976).
- ⁸S. Brunner and E. Valeo, "Simulations of electron transport in laser hot spots," *Phys. Plasmas* **9**(3), 923–936 (2002).
- ⁹R. C. Davidson, D. A. Hammer, I. Haber, and C. E. Wagner, "Nonlinear development of electromagnetic instabilities in anisotropic plasmas," *Phys. Fluids* **15**(2), 317–333 (1972).
- ¹⁰R. Duclous, B. Dubroca, F. Filbet, and V. Tikhonchuk, "High order resolution of the Maxwell–Fokker–Planck–Landau model intended for icf applications," *J. Comput. Phys.* **228**(14), 5072–5100 (2009).
- ¹¹C. T. Dum, "Anomalous heating by ion sound turbulence," *Phys. Fluids* **21**(6), 945–955 (1978).
- ¹²C. T. Dum, "Anomalous electron transport equations for ion sound and related turbulent spectra," *Phys. Fluids* **21**(6), 956–969 (1978).
- ¹³E. M. Epperlein and R. W. Short, "A practical nonlocal model for electron heat transport in laser plasmas," *Phys. Fluids B* **3**(11), 3092–3098 (1991).
- ¹⁴B. D. Fried, "Mechanism for instability of transverse plasma waves," *Phys. Fluids* **2**(3), 337 (1959).
- ¹⁵M. J. Keskinen, "Fully kinetic Fokker–Planck model of thermal smoothing in nonuniform laser-target interactions," *Phys. Rev. Lett.* **103**(5), 055001 (2009).
- ¹⁶M. J. Keskinen, "Kinetic model for ion pressure perturbations in inhomogeneous laser-matter interactions," *Phys. Plasmas* **17**(5), 054507–054507–4 (2010).
- ¹⁷R. J. Kingham and A. R. Bell, "An implicit Vlasov–Fokker–Planck code to model non-local electron transport in 2-d with magnetic fields," *J. Comput. Phys.* **194**(1), 1–34 (2004).
- ¹⁸R. J. Kingham and A. R. Bell, "Nonlocal magnetic-field generation in plasmas without density gradients," *Phys. Rev. Lett.* **88**(4), 045004 (2002).
- ¹⁹A. Bruce Langdon, "Nonlinear inverse bremsstrahlung and heated-electron distributions," *Phys. Rev. Lett.* **44**(9), 575–579 (1980).
- ²⁰J. F. Luciani, P. Mora, and J. Virmont, "Nonlocal heat transport due to steep temperature gradients," *Phys. Rev. Lett.* **51**(18), 1664–1667 (1983).
- ²¹A. Marocchino, M. Tzoufras, S. Atzeni, A. Schiavi, Ph. D. Nikolai, J. Mallet, V. Tikhonchuk, and J.-L. Feugeas, "Comparison for non-local hydrodynamic thermal conduction models," *Phys. Plasmas* **20**, 022702 (2013).
- ²²J. P. Matte and J. Virmont, "Electron heat transport down steep temperature gradients," *Phys. Rev. Lett.* **49**(26), 1936–1939 (1982).
- ²³J. P. Matte, M. Lamoureux, C. Møller, R. Y. Yin, J. Delettrez, J. Virmont, and T. W. Johnston, "Non-Maxwellian electron distributions and continuum x-ray emission in inverse bremsstrahlung heated plasmas," *Plasma Phys. Controlled Fusion* **30**(12), 1665 (1988).
- ²⁴K. Molvig, "Filamentary instability of a relativistic electron beam," *Phys. Rev. Lett.* **35**(22), 1504–1507 (1975).
- ²⁵B. Reville and A. R. Bell, "Universal behaviour of shocks in the presence of efficient cosmic-ray acceleration," *Mon. Not. R. Astron. Soc.* **430**(4), 2873–2884 (2013).
- ²⁶M. N. Rosenbluth, W. M. MacDonald, and D. L. Judd, "Fokker–Planck equation for an inverse-square force," *Phys. Rev.* **107**(1), 1–6 (1957).
- ²⁷L. Spitzer and R. Härm, "Transport phenomena in a completely ionized gas," *Phys. Rev.* **89**(5), 977–981 (1953).
- ²⁸A. Sunahara, J. A. Delettrez, C. Stoeckl, R. W. Short, and S. Skupsky, "Time-dependent electron thermal flux inhibition in direct-drive laser implosions," *Phys. Rev. Lett.* **91**(9), 095003 (2003).
- ²⁹A. G. R. Thomas, R. J. Kingham, and C. P. Ridgers, "Rapid self-magnetization of laser speckles in plasmas by nonlinear anisotropic instability," *New J. Phys.* **11**(3), 033001 (2009).
- ³⁰A. G. R. Thomas, M. Tzoufras, A. P. L. Robinson, R. J. Kingham, C. P. Ridgers, M. Sherlock, and A. R. Bell, "A review of Vlasov–Fokker–Planck numerical modeling of inertial confinement fusion plasma," *J. Comput. Phys.* **231**(3), 1051–1079 (2012).
- ³¹M. Tzoufras, C. Ren, F. S. Tsung, J. W. Tonge, W. B. Mori, M. Fiore, R. A. Fonseca, and L. O. Silva, "Stability of arbitrary electron velocity distribution functions to electromagnetic modes," *Phys. Plasmas* **14**(6), 062108 (2007).
- ³²M. Tzoufras, A. R. Bell, P. A. Norreys, and F. S. Tsung, "A Vlasov–Fokker–Planck code for high energy density physics," *J. Comput. Phys.* **230**(17), 6475–6494 (2011).
- ³³E. S. Weibel, "Spontaneously growing transverse waves in a plasma due to an anisotropic velocity distribution," *Phys. Rev. Lett.* **2**(3), 83–84 (1959).
- ³⁴The algorithm for the isotropic self-collision operator transitions from utilizing the full distribution function to employing its Taylor-expansion as $p \rightarrow 0$. The CFL condition slightly varies, depending on the location where this transition occurs.
- ³⁵Summation over repeated indices is assumed, $\varepsilon_{ijk} = 1$ if (i, j, k) is an even permutation of (x, y, z) , $\varepsilon_{ijk} = -1$ if it is an odd permutation, and 0 if it has repeated indices.